The Meteoritical Society

Meteoritics & Planetary Science 49, Nr 7, 1141–1156 (2014)
doi: 10.1111/maps.12320

Characterization of weathering and heterogeneous mineral phase distribution in brachinite Northwest Africa 4872

Brendt C. HYDE[1*], James M. D. DAY[2], Kimberly T. TAIT[1], Richard D. ASH[3], David W. HOLDSWORTH[4], and Desmond E. MOSER[5]

[1]Department of Natural History, Mineralogy, Royal Ontario Museum, Toronto, Ontario M5S 2C6, Canada
[2]Geosciences Research Division, Scripps Institution of Oceanography, La Jolla, California 92093–0244, USA
[3]Department of Geology, University of Maryland, College Park, Maryland 20742, USA
[4]Robarts Research Institute, Imaging Research Laboratories, London, Ontario N6A 5K8, Canada
[5]Department of Earth Sciences, Western University, London, Ontario N6A5B7, Canada
[*]Corresponding author. E-mail: brendth@rom.on.ca

(Received 28 January 2013; revision accepted 29 April 2014)

Abstract–Terrestrial weathering of hot desert achondrite meteorite finds and heterogeneous phase distributions in meteorites can complicate interpretation of petrological and geochemical information regarding parent-body processes. For example, understanding the effects of weathering is important for establishing chalcophile and siderophile element distributions within sulfide and metal phases in meteorites. Heterogeneous mineral phase distribution in relatively coarsely grained meteorites can also lead to uncertainties relating to compositional representativeness. Here, we investigate the weathering and high-density (e.g., sulfide, spinel, Fe-oxide) phase distribution in sections of ultramafic achondrite meteorite Northwest Africa (NWA) 4872. NWA 4872 is an olivine-rich brachinite ($Fo_{63.6 \pm 0.5}$) with subsidiary pyroxene ($Fs_{9.7 \pm 0.1}Wo_{46.3 \pm 0.2}$), Cr-spinel (Cr# = 70.3 ± 1.1), and weathered sulfide and metal. Raman mapping confirms that weathering has redistributed sulfur from primary troilite, resulting in the formation of Fe-oxide (-hydroxide) and marcasite (FeS_2). From Raman mapping, NWA 4872 is composed of olivine (89%), Ca-rich pyroxene (0.4%), and Cr-spinel (1.1%), with approximately 7% oxidized metal and sulfide and 2.3% marcasite-dominated sulfide. Microcomputed tomography (micro-CT) observations reveal high-density regions, demonstrating heterogeneities in mineral distribution. Precision cutting of the largest high-density region revealed a single 2 mm Cr-spinel grain. Despite the weathering in NWA 4872, rare earth element (REE) abundances of pyroxene determined by laser-ablation inductively coupled plasma mass spectrometry (LA-ICP-MS) indicate negligible modification of these elements in this mineral phase. The REE abundances of mineral grains in NWA 4872 are consistent with formation of the meteorite as the residuum of the partial melting process that occurred on its parent body. LA-ICP-MS analyses of sulfide and alteration products demonstrate the mobility of Re and/or Os; however, highly siderophile element (HSE) abundance patterns remain faithful recorders of processes acting on the brachinite parent body(ies). Detailed study of weathering and phase distribution offers a powerful tool for assessing the effects of low-temperature alteration and for identifying robust evidence for parent-body processes.

INTRODUCTION

Achondrites produced by partial melting of chondritic precursors, such as acapulcoite-lodranites, brachinites, ureilites, and primitive enstatite achondrites (e.g., McCoy et al. 1997; Rankenburg et al. 2008; Izawa et al. 2011), offer insight into the key stages of asteroidal melting and differentiation in the early solar system. In particular, brachinites are thought to be the residuum after partial melting of an asteroidal body

(e.g., Day et al. 2009, 2012a; Goodrich 1998). Recently, brachinites have been linked to the oligoclase-rich achondrite meteorites Graves Nunataks 06128 and 06129 (hereafter referred to as GRA 06128/9; Day et al. 2009, 2012a; Shearer et al. 2010; Zeigler et al. 2008; Wang et al. 2014). It has been suggested that partial melting could have produced both derivative felsic-melts, such as GRA 06128/9, as well as olivine-rich residuum, represented by brachinites.

Multiple splits from single brachinites exhibit differences in bulk HSE (Os, Ir, Ru, Rh, Pt, Pd, Re, Au) abundances, reflecting the effects of heterogeneous phase distribution, grain size, and, in some cases, uneven weathering (Day et al. 2012a). Weathering is a crucial issue when dealing with hot desert meteorite finds because it can obscure primary information on parent-body processes (e.g., Crozaz et al. 2003). Past work has also reported major-, minor-, and trace element mobilization in multiple meteorite groups, including chondrites (e.g., Ash and Pillinger 1995; Lee and Bland 2004; Al-Kathiri et al. 2005), ureilites (Goodrich and Lugmair 1995; Guan and Crozaz 2000), and in lunar meteorites (Zeigler et al. 2006) exposed to hot desert weathering. Observed chemical modifications include an increase in Ca, Ba, Sr, U, Pb, and As abundances, as well as an increase in the light rare earth elements (LREE) relative to the heavy REE (HREE). Mobilization of sulfur from sulfides has also been noted for some hot desert meteorite finds (e.g., Lee and Bland 2004).

In this study, a detailed petrological assessment is made of North West Africa (NWA) 4872 to understand how low-temperature terrestrial alteration and heterogeneous modal phase distribution affects primary chemical information about parent-body processes retained in the meteorite. In particular, this study focuses on the effect of sulfide and metal alteration on HSE abundances in meteorite samples. NWA 4872 contains no observable plagioclase (Rumble et al. 2008) and has the lowest REE abundance of any measured brachinite (Day et al. 2012a) making it the current endmember representative of the residuum formed from the partial melting process on its parent body and thus an important meteorite for comparison with other brachinites. Detailed Raman spectroscopy, laser-ablation inductively coupled plasma–mass spectrometry (LA-ICP-MS) trace element abundance data, and high-resolution backscatter electron (BSE) imaging of weathering products, as well as micro-CT and mapping of phase distribution, in NWA 4872 are reported. Such a combined analytical approach allows for refined understanding of mineral-scale variations in NWA 4872, and the effect of weathering on bulk chemistry and mineralogy. This work has implications for studying weathering products in other olivine and/or pyroxene-dominated meteorites and evaluates methods for studying weathering products.

MATERIALS AND METHODS

Northwest Africa 4872

Brachinite NWA 4872 was found in Algeria in 2007 and officially classified in 2008 (Connolly et al. 2007; Weisberg et al. 2008). The bulk of NWA 4872 consists of a stone broken into two portions, weighing a total of 2.87 kg. The main mass and research fragments are part of the Royal Ontario Museum's meteorite collection. The study material was cut from an area close to the exterior (i.e., an "end-cut"), which is typical for use in thin section and bulk analytical work. This study used a probe mount with a surface area of 153 mm^2 (hereafter referred to as ROMB-1) and the remaining 23.55 g end-cut of NWA 4872. The end-cut was subsequently sectioned to produce a mount with a surface area of 238 mm^2 (ROMB-2).

Micro-CT Imaging and Precision Cutting

Micro-CT scans were run on the 23.55 g piece of NWA 4872 to observe volume, bulk density, and variations in internal density. Volume and bulk density measurements used a GE Locus Ultra with an X-ray peak voltage of 120 kVp, current of 20 mA, and isotropic voxel spacing of 154 μm. High tube voltage and added filtration (0.15 mm Cu) minimized the effects of beam hardening. Higher resolution scans of internal density variations used a GE Explore SpecCZT with a peak voltage of 110 kVp, current of 32 mA and an isotropic voxel spacing of 50 μm. A software correction for residual beam-hardening artifact was applied in postprocessing, based on a semi-empirical correction scheme (Herman 1979). Three dimensional viewing and analysis used the MicroView 2.1.2 (GE Healthcare). The auto threshold feature in MicroView (see Otsu 1979) determined the gray-scale intensity for 3-D surface segmentation and subsequent analysis. Surface reconstruction was necessary for volume determination and for correlating surface features with interior areas of interest. Precision cutting to expose an area of interest, from Micro-CT observation, used a Wells 6234 diamond-wire saw with a 0.5 mm wire. The sample was dry-cut and the powder produced was collected, resulting in minimal sample loss.

Backscatter Electron Imaging

Imaging used a Hitachi SU6600 variable pressure, analytical field emission gun scanning electron

microscope (SEM) with a five-sector solid state BSE detector. Image mosaics were constructed to observe large-scale textural features and modal values. Threshold values for the phases were determined visually by observing grain boundaries. Image processing for all modal analyses used the program Image J (Rasband 2012).

In addition to standard BSE imaging, collection of high-resolution images of an unidentified Fe-phosphate phase was necessary to place the phase in textural context. The region was first milled using a Leo 1540XB focused ion beam (FIB) with a 30 kV accelerating voltage and 1 nA beam current. Gallium ions sputtered the surface at a glancing angle of 4°. The process was monitored in real time to observe any sample changes during the process. High-resolution BSE images were then taken at a low accelerating voltage (5 kV) and a beam current of 2.3 nA as electron channeling can occur under these conditions, highlighting structural variations within the phase.

X-Ray Mapping

X-ray maps were acquired using an FEI Quanta 200 environmental scanning electron microscope. Mapping used an EDAX SiLi detector with a superultrathin window and was done in low vacuum (70 Pa) to minimize volatilization from weathering products during the initial survey. Mapping used accelerating voltages of 17–20 kV, working distances of 9.8–10.1 mm, step size of 6.6 μm, and a dwell time of 400 μs at each spot. These maps were used to observe mineral distribution and to locate phases for further analysis.

Raman Spectroscopy

Raman spectra were acquired using a Horiba LabRAM Aramis micro-Raman spectrometer. A 532 nm, 50 mW laser was used, but was filtered to 10% power to prevent sample damage. The power output on the sample surface was approximately 1.6 mW μm^{-2}. A 1200 g mm^{-1} grating and 150 μm slit were used during collection. A Si reference material was used for calibration and spectra were collected from 100 cm^{-1} to 3800 cm^{-1}. Two spectra were collected for 50 s at each point and the results were averaged. The RRUFF Raman database and CrystalSleuth (Laetsch and Downs 2006) were used for rapid identification, followed by literature comparisons.

Detailed Raman maps were created by rastering the laser across an area. For modal calculations, maps of various sizes and spatial resolutions were made (see Table 1) and two spectra were collected for 1.5 s at each point. The average spectrum was linked to its corresponding point. A 50× long working distance objective and autofocus function were used, to map surface areas larger than typically possible with Raman systems. Analysis and processing of spectra and maps used LabSpec 6. For modal determinations, spectra were baseline corrected and threshold values for each phase were determined by comparing the maps with grain boundaries in optical images and by observing spectra near the proposed threshold values.

Electron Backscatter Diffraction

Electron backscatter diffraction (EBSD) was used to help confirm mineral identifications. The Hitachi SU6600 system described previously was used in conjunction with an Oxford Instruments Nordlys EBSD detector. Following observations made on the Fe-phosphate, the sample was polished using 0.05 μm alumina powder in oil. During analysis the sample mount was tilted to 70° and raised to a working distance of 19 mm. A 20 kV, 6 nA electron beam was used to generate Kikuchi bands and Oxford HKL Channel 5 software was used for indexing. A range of 5–7 detected bands were required for identification, which were detected using band centers.

Electron Microprobe Analysis

Electron microprobe (EMP) analysis using wavelength dispersive spectroscopy was conducted on a Cameca SX-50 instrument. All analyses used a 1 μm beam. For silicates, an accelerating voltage of 15 kV and beam current of 15 nA were used. Sulfide analyses used settings of 20 kV and 50 nA, while Cr-spinel and Fe-oxide analyses used settings of 20 kV and 25 nA. Prior to Cr-spinel analysis, possible interference between Ti Kβ and V Kα was checked using a standard spinel of similar composition. Use of an interference correction did not change the resulting concentrations beyond the accepted uncertainty levels, indicating that corrections were unnecessary. Phosphates were analyzed using a JEOL JXA-8230 equipped with five wavelength dispersive spectrometers. An accelerating voltage of 15 kV and 5 nA beam current were used. A spot size of 5 μm was used for all phosphate analyses except for merrillite, which used a spot size of 3 μm due to merrillite's small grain size. The halides were measured first with a low beam current and defocused beam to minimize mobilization. A time dependent intensity correction was not applied as the magnitude of this correction was below that of the error associated with counting statistics at these concentrations. Synthetic fluorophlogopite was used as the standard for F and scapolite was used for Cl.

Table 1. Modal mineralogy determinations for NWA 4872 (wt%, ±1σ standard deviation).

	Dimensions (mm)	Step size (μm)	Olivine	Pyroxene	Cr-spinel	Sulfide	Fe-oxide	Goethite	High-density phases
BSE threshold method									
ROMB-1	17 × 9		90	1					9
ROMB-2	17 × 14		89	1					10
Raman maps									
ROMB-1	14.3 × 5.0	200	90	0.4	1.4	1.1	7	0.4	10
ROMB-1	8.5 × 0.9	15	89	0.6	1.2	2.2	6	0.3	9
Avg. ROMB-1			90 ± 2	0.5 ± 0.1	1.3 ± 0.2	1.6 ± 0.6	7 ± 1	0.4 ± 0.1	10
ROMB-2	14.3 × 5.0	200	88	0.4	0.7	2.8	8	0.1	12
ROMB-2	4.9 × 1.4	15	88	0.3	1.2	3.2	8	0.2	12
Avg. ROMB-2			88 ± 1	0.3 ± 0.1	1.0 ± 0.3	3.0 ± 0.5	8 ± 1	0.1 ± 0.1	12
Avg. Raman			89 ± 1	0.4 ± 0.1	1.1 ± 0.3	2.3 ± 0.9	7 ± 1	0.2 ± 0.1	10

High-density phases include Cr-spinel, sulfide, and Fe-oxide. The minor amount of goethite could not be resolved using the backscatter electron (BSE) threshold method. Small amounts of chlorapatite, merrillite, anhydrite, calcite, and magnesium sulfate were observed during mapping, but amounts were too small for quantification. ROMB-2 Raman maps do not include the large Cr-spinel grain (0.8% of section).

LA-ICP-MS Analysis

A New Wave Research UP213 (213 nm) laser-ablation system coupled to a Thermo-Finnigan Element 2 ICP-MS was used to establish minor and trace element abundances in mineral phases. Olivine, pyroxene, chlorapatite, Cr-spinel, Fe-sulfide, and Fe-oxide were analyzed using spots of 12–80 μm, a laser repetition rate of 7 Hz, and photon fluence of 1.5–2.6 J cm^{-2}. The ablation cell was flushed with He gas flow of 1 L min^{-1} to transport ablated material to a mixing volume where an additional 0.4 L min^{-1} of Ar was introduced before reaching the torch. Data collection consisted of approximately 20 s of gas background, approximately 40 s of laser ablation, and a washout time >120 s between spots. Data were collected as a time series. Integration intervals for the gas background and sample analysis were selected using LAMTRACE software (Achterberg et al. 2001). Each LA-ICP-MS analysis was normalized to CaO (silicates and phosphates), FeO (Fe-oxides), and Fe (sulfides) as measured by EMP. Replicate LA-ICP-MS analyses of the BHVO glass standard, run twice at the beginning and end of analytical sessions for 2–12 unknowns, yielded an external precision of better than ±8.2% (2σ relative standard deviation) for all measured trace element and major element compositions in silicates and phosphates. Replicate LA-ICP-MS analyses of the internal reference material, JBS sulfide, run twice at the beginning and end of analysis of 11 unknowns of Fe-oxides, Cr-spinel, and sulfides, yielded external precision of better than ±6% (2σ relative standard deviation) for HSE abundances.

RESULTS

3-D Imaging and Precision Cutting

The 23.55 g piece of NWA 4872 was imaged using Micro-CT (Fig. 1) and has a calculated volume of 6.58 ± 0.02 cm^3 and bulk density of 3.58 ± 0.01 g cm^{-3}. The volume measurements used CT scans from two different meteorite orientations to confirm reproducibility and uncertainty was inferred from these measurements. Similar uncertainty values were established in prior CT work on meteorites (McCausland et al. 2010). Bulk properties could only be measured with the lower resolution scans of NWA 4872. Artifacts around edges in the higher resolution scans did not allow for these calculations, but these scans did offer a better view of internal density variations highlighting a heterogeneous distribution of high-density grains (Fig. 1). Discriminating between the high-density phases (Cr-spinel, Fe-sulfide, and Fe-oxide) in these CT-images is not possible. The meteorite volume constructed from the micro-CT data allowed for correlation between external surface features and internal areas of interest, making it possible to cut through a 2 mm high-density region. The cut exposed a Cr-spinel grain 2 mm across (Fig. 1). Subsequently a new polished section of this exposure was made for further analysis (ROMB-2).

General Petrology

Reflected light and SEM observations were conducted on ROMB-1 and ROMB-2 to document petrologic features. Olivine is the most abundant silicate

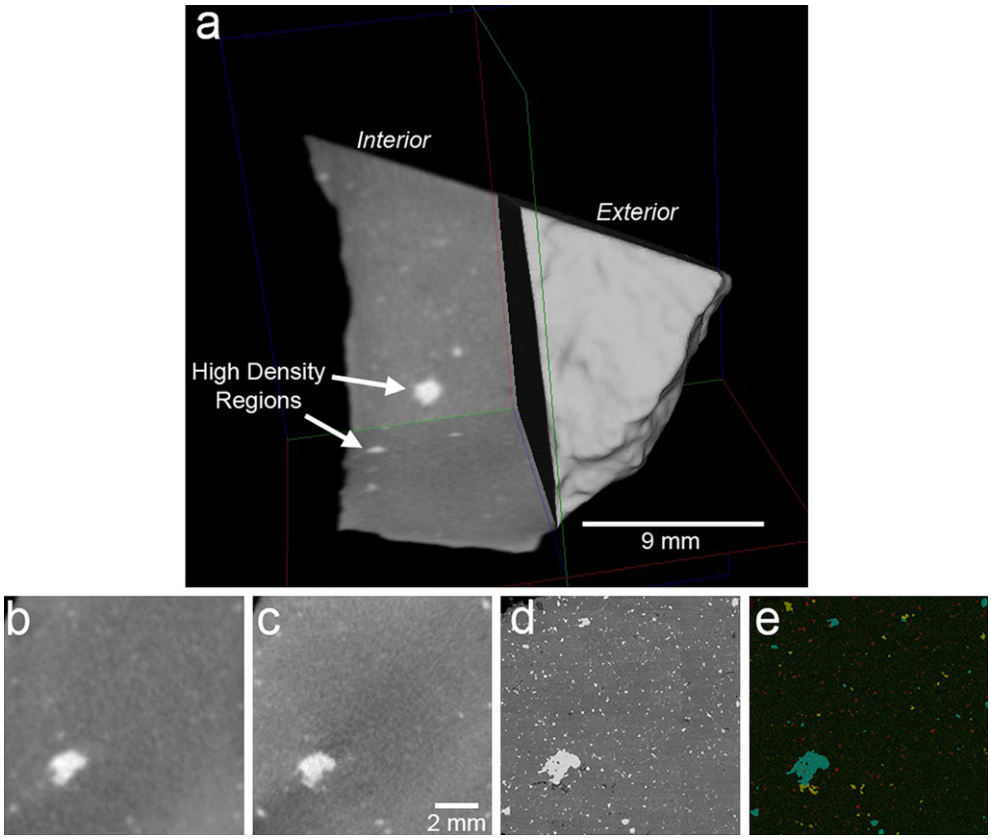

Fig. 1. a) Micro-CT image of NWA 4872 showing exterior topography and interior heterogeneous distribution of high-density phases. Planes shown represent virtual cuts into the sample. Images shown in b-e are the same scale and focus on a region (b) of high density seen within the micro-CT at 154 μm resolution. c) Shows the same area at 50 μm micro-CT resolution, and d) is a backscatter electron (BSE) image of the same region following the precision cut. An elemental map (e) showing Cr (blue), S (red), Ca (yellow), and Fe (green) shows the high-density phase to be a Cr-spinel.

in the sections and has a range in cross section from approximately 10 μm to over 800 μm across. Rumble et al. (2008) describes a bimodal distribution in grain size in NWA 4872, while the sections examined here contain a more continuous distribution. Pyroxene grains are commonly approximately 50 μm across and Cr-spinel grains typically measure 100–300 μm across, with the exception of the 2 mm long Cr-spinel grain in ROMB-2 (see above). Fe-sulfide and Fe-oxide (-hydroxide) were both observed as small micron-sized veins surrounding the bulk silicates and as regions with cross sections of tens of microns across. Chlorapatite is present as a minor phase and is sometimes associated with merrillite, Fe-phosphate, and/or anhydrite. As with a prior study (Rumble et al. 2008), no plagioclase was observed in the polished mounts that we studied.

Textual features include olivine triple-junctions (Fig. 2) in many areas—consistent with equilibration, quasi-parallel fractures in ROMB-1 (Fig. 2) and inclusions a few microns in diameter in the silicates and Cr-spinel. The inclusions are often roughly circular in cross section and usually contain sulfide and/or metal, although phosphate and silicate inclusions are also present. The sulfide and metal inclusions are often grouped together and occasional large populations of inclusions are seen near veins and grain boundaries. These inclusions are the only sulfide and metal not extensively altered by weathering. ROMB-2 contains a larger abundance of sulfide/metal inclusions and contains slightly more sulfide in general.

Texture of Fe-Phosphate Phase at High Resolution

The ion milling done prior to high-resolution SEM imaging did not result in any cracks or volume changes in the potentially volatile-rich Fe-phosphate. SEM images suggest that the unknown Fe-phosphate phase is a fine-grained weathering product or a shock melt product (Fig. 3). Metal and Fe-sulfide surrounding the phosphate phases are weathered. When analyzed using EBSD, no diffraction pattern was obtained from the Fe-phosphate. This indicates that the material is either

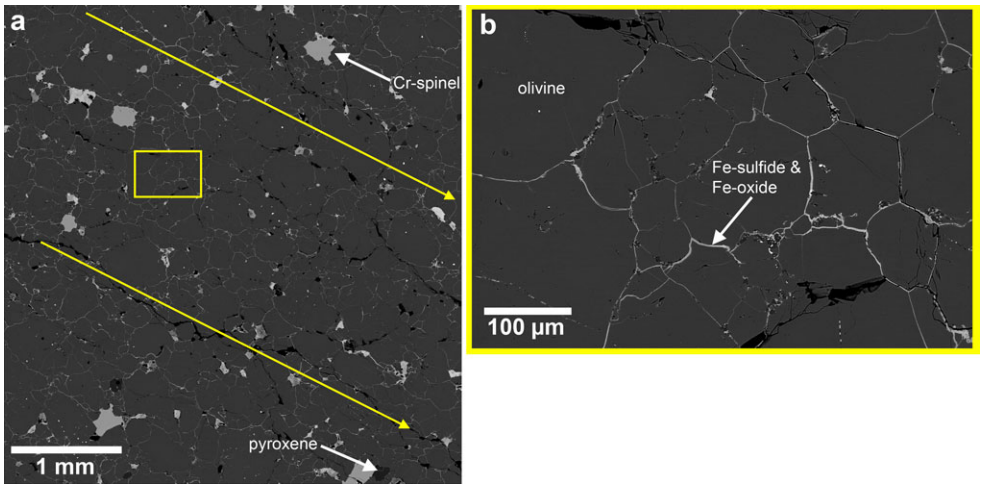

Fig. 2. a) Backscatter electron (BSE) mosaic showing quasi-parallel fractures that occur in ROMB-1 (yellow arrows show direction). In the BSE image, dark gray regions are areas of olivine with minor Ca-rich pyroxene and lighter regions are areas of Cr-spinel and regions of sulfide and metal alteration. b) Highlighted region in (a) illustrating dark olivine grains surrounded by Fe-sulfide and Fe-oxide (-hydroxide) (lighter-colored boundaries between grains). Triple-junctions and rounded olivine grains are found in most regions of NWA 4872. (see online version for color figure.)

amorphous or, more likely, an assemblage of nanocrystalline grains each of which is smaller than the approximately 100 nm spatial resolution of the technique. Neighboring mineral grains of the NWA 4872 assemblage (e.g., chlorapatite) did, however, return clear electron diffraction patterns, and thus the absent or unresolvable electron diffraction may be a characteristic of the complex interstitial phosphate/sulfide mineral assemblages in NWA 4872.

Mineral Identification

Raman analysis confirmed that marcasite [FeS_2] is the dominant Fe-sulfide in the sections studied and identified weathering products (hematite, magnetite, and goethite) associated with the sulfide. Merrillite and anhydrite were also confirmed by Raman analysis and the Fe-phosphate phase was examined. A minor amount of Mg-sulfate was also detected. Olivine, pyroxene, Cr-spinel, and chlorapatite were also analyzed by Raman; however, these phases are identified by other methods (e.g., EMP) and are not discussed further. The peak values found for the phases in this study are given in Fig. 4. For comparisons of these spectra with the RRUFF database and for details of the combined Raman and EBSD characterization technique, please refer to the supporting information. The marcasite peak locations in this study match past work by White (2008) (323 and 386 cm^{-1}). However, we do not see the minor peak at 532 cm^{-1} observed by Mernagh and Trudu (1993). We also report peaks at 342 cm^{-1}, 427 cm^{-1}, and a peak overlapping the 386 cm^{-1} peak at about 380 cm^{-1}. These could be attributed to pyrrhotite (Wang et al. 1999: strongest peak for standard pyrrhotite at 341 cm^{-1}) and/or pyrite (White 2008: 343, 379, and 430 cm^{-1}), although pyrite is highly unusual in meteorites. Generally, the spectral contribution from pyrrhotite/pyrite is low, but areas richer in these phases do occur (Fig. 4, marcasite and pyrrhotite/pyrite). Marcasite was confirmed by EBSD and a pyrrhotite group mineral was also identified in veins and inclusions. Unfortunately, areas with the two phases intimately mixed, as observed in the Raman data, were not confirmed through EBSD.

Attempts to analyze unaltered Fe-sulfide found as inclusions resulted in spectra with one very weak broad group of peaks between 180 and 380 cm^{-1}, with a high point near 335 cm^{-1} and second point sometimes occurring at 230 cm^{-1}. Variability in structure and Fe-S ratios in pyrrhotite result in a number of unique Raman patterns (see Wang et al. 1999). At present, the available Raman spectral libraries are incomplete with regard to sulfides and, for this reason, no definitive identification can be made by Raman alone.

The magnetite peak locations here correspond well with spectra taken from synthetic material (Wang et al. 2004: 305, 539, and 667 cm^{-1}). There is a great deal of discrepancy in the literature regarding peak positions and widths for iron oxides and oxyhydroxides, due to laser power dependence (de Faria et al. 1997). The peak positions reported here will only match those collected at similar laser power. Magnetite spots were also confirmed by EBSD.

For hematite, the Raman peaks reported here match well with the peaks recorded in Wang et al. (2004) (223, 241, 289, 404, 491, 608, 659, and

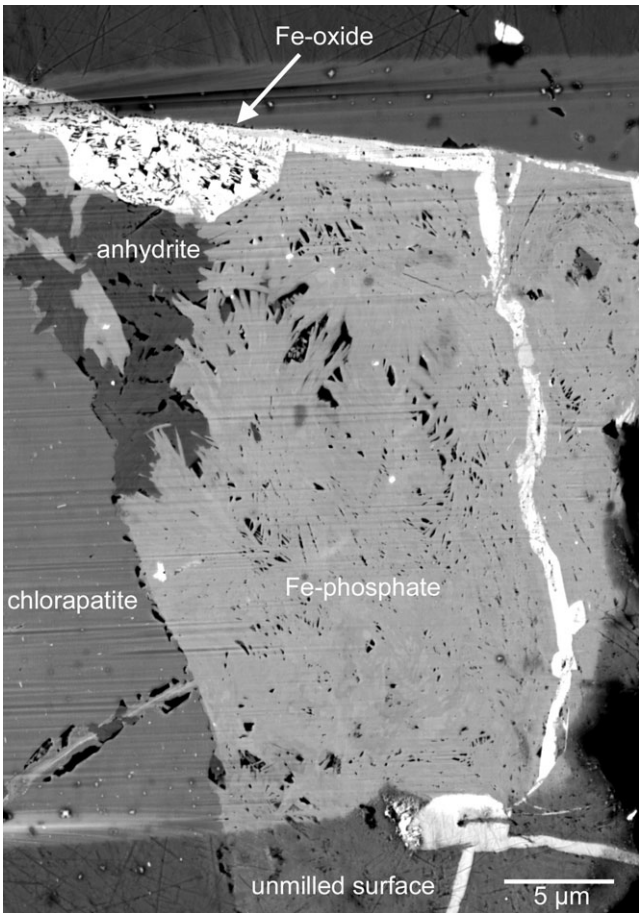

Fig. 3. Low kV backscatter image of focused ion beam milled surface of Fe-phosphate phase.

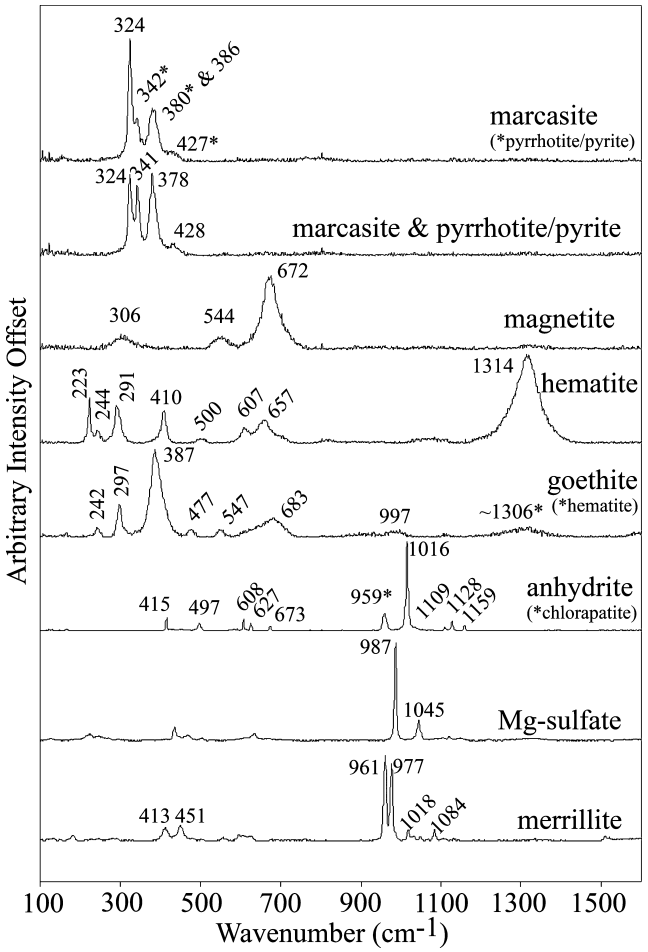

Fig. 4. Raman spectra of weathering products and merrillite in NWA 4872. Starred peak values represent minor contributions from other minerals.

1305 cm^{-1}) and, for the most part, are within the range of values given in de Faria et al. (1997). The goethite peaks match de Faria et al. (1997) and de Faria and Lopes (2007) (243, 299, 385, 479, 550, 685, and 993 cm^{-1}). A small broad peak at approximately 1306 cm^{-1} is related to a small amount of hematite.

Both anhydrite and Fe-phosphate are found near the chlorapatite in NWA 4872. Anhydrite closely matches the major peaks in Sharma et al. (2009) (417, 501, 611, 629, 677, 1018, 1099, 1130, and 1162 cm^{-1}). Our study also includes a peak at 959 cm^{-1} related to surrounding chlorapatite (matching the major apatite peak in Cooney et al. 1999). The Fe-phosphate has weak peaks, some of which could arguably be resulting from scatter off surrounding phases, meaning the spectrum may not be completely representative of a single phase. However, the spectrum appears broadly similar to other hydrated Fe-phosphates (see supporting information). This, alongside elemental data, suggests that the term phosphate is appropriate.

In a few locations, magnesium sulfate of various hydration states has formed as a result of weathering. The material has two main peaks that vary in intensity relative to each other. The first peak is consistent with past work on both epsomite [$MgSO_4 \cdot 7H_2O$] and hexahydrite [$MgSO_4 \cdot 6H_2O$] (Wang et al. 2006: 984.1 and 983.6 cm^{-1} respectively). The second peak is consistent with kieserite [$MgSO_4 \cdot H_2O$] (Wang et al. 2006: 1046.1 cm^{-1}). Low-level peaks, seen in some areas, between these two main peaks suggest that magnesium sulfate of intermediate hydration states is also present (Wang et al. 2006) and groupings of minor peaks from 224 to 269, 436 to 469, 611 to 669, and 1087 to 1148 cm^{-1} are also consistent with the presence of multiple hydration states (Wang et al. 2006). A peak at 1217 cm^{-1} is from the kieserite present (Wang et al. 2006: 1215 cm^{-1}). A minor peak at 505 cm^{-1} is not obviously attributed to magnesium sulfate. Magnesium sulfates can change hydration states simply through changes in relative humidity at room temperature (see Chou and Seal 2003). This ease in hydration and

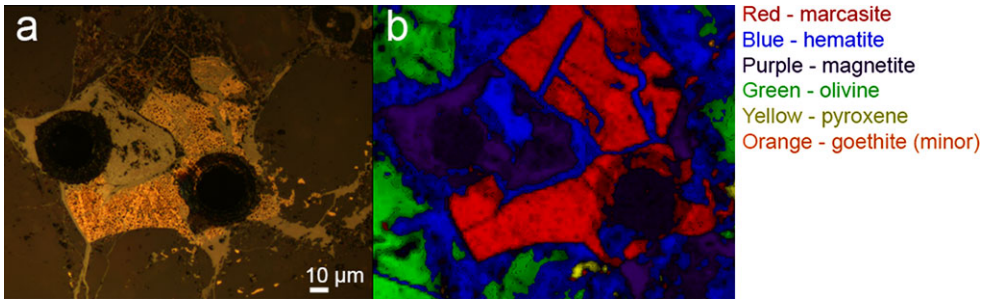

Fig. 5. a) Optical image of a target for Raman mapping in NWA 4872. b) Raman map of a weathered sulfide grain. Colors correspond to the spectra measured in the position of each pixel. The large black circles are laser-ablation pits. The left spot was positioned in a magnetite-dominated region and the right spot was positioned in a marcasite-dominated region.

dehydration is clearly visible in the material observed in this study.

Finally, we identified merrillite found at the edges of some of the chlorapatite. The spectrum for merrillite can be quite variable, as a function of REE content (Jolliff et al. 2006). The major peaks in this study match those of Cooney et al. (1999) (410, 448, 958, 974, 1028, and 1082 cm^{-1}). This study did not see a peak near 923 cm^{-1}, consistent with merrillite and not whitlockite (Jolliff et al. 2006) or bobdownsite [$Ca_9Mg(PO_4)_6(PO_3F)$] (Tait et al. 2011).

Mineralogical Mapping and Modal Abundances

There is close agreement between the modal abundances obtained by the BSE threshold method (cf. Day et al. 2006a) and from Raman mapping (Table 1—modal abundances determined by Raman are cross sectional area percents and determinations for ROMB-2 did not include the large Cr-spinel grain). The Raman mapping provides greater resolution of high-density mineral phases, identifies weathering products, and provides information on mixtures. In general, NWA 4872 sections are composed of olivine (89%; see Table 1) with minor high-Ca pyroxene (0.4%). Cr-spinel grains typically represent 1.1% (although in the case of ROMB-2 the single 2 mm long Cr-spinel grain makes up 0.8% of the section in the cut that we made). Fe-oxide (-hydroxide) alteration comprises approximately 7% and sulfide comprises 2.3% of NWA 4872. The phosphate and sulfate were too minor to include in modal calculations. Threshold values for each phase in the Raman maps had to be determined visually, which includes observational bias. However, two modal determinations were made on two maps per section to help smooth observational effects. Errors given are the standard deviations of the four measurements taken for each section and the overall average and error include all eight values. In most cases, mineral phases have a great deal of contrast in their Raman spectra. However, the short collection times required for mapping and the imperfect surfaces of the Fe-oxides typically resulted in low intensity, leading to greater uncertainty. Additionally, the Cr-spinel and magnetite spectra are quite similar leading to spectral overlap. Peak positions are far enough apart that definitive identification is possible. However, the low intensity of the magnetite in these maps did result in some uncertainty. In NWA 4872 sections, the magnetite was intimately mixed with hematite, so our search used a combined spectrum ("Fe-oxide") to minimize problems associated with the Cr-spinel overlap.

Detailed Raman maps of Fe-sulfide and oxide grains provided information on terrestrial weathering (Fig. 5). The marcasite-dominated sulfide is associated with hematite, magnetite, and goethite. Unmounted cut surfaces of the meteorite contained these sulfide weathering phases and textures proving they were not related to sample preparation. Weathering pathways clearly show the preferential degradation of Fe-sulfide and metal, but no significant weathering of the silicates was observed. Calcite was observed on the outside of the 23.55 g piece and in cracks of polished-section ROMB-1.

Major-Element Composition

Quantitative EMP analysis of the major-element compositions of silicates and Cr-spinel (Table 2) in NWA 4872 are similar to those reported by Rumble et al. (2008). Silicates are compositionally homogeneous with olivines of $Fo_{63.6 \pm 0.5}$ (n = 64), and high-Ca pyroxene with $Fs_{9.7 \pm 0.1}Wo_{46.3 \pm 0.2}$ (n = 54). Rumble et al. (2008) reported $Fo_{64.9}$ for olivine, and $Fs_{10.3}Wo_{47}$ from high-Ca pyroxene, but the total number of grains/analyses made in that study were not reported. The Cr-spinel composition (Cr# = 70.3 ± 1.1, Cr# = Cr/[Cr+Al] in mole%, n = 50) is consistent with the range reported for brachinites in Rumble et al. (2008); however, they report the composition for NWA 4872 as Cr# = 74.

Table 2. Composition of primary minerals in NWA 4872 (wt%, ±1σ standard deviation).

	Olivine (n = 64)	Pyroxene (n = 54)	Cr-spinel (n = 50)	Chlorapatite (n = 11)	Merrillite (n = 3)
SiO_2	36.4 ± 0.2	53.5 ± 0.3	0.16 ± 0.04	0.26 ± 0.03	0.2 ± 0.2
P_2O_5	–	–	–	41.0 ± 0.4	45.8 ± 0.3
Na_2O	n.d.	0.44 ± 0.03	–	0.42 ± 0.03	2.9 ± 0.1
MgO	31.2 ± 0.4	15.5 ± 0.1	4.72 ± 0.2	0.02 ± 0.03	3.41 ± 0.02
Al_2O_3	n.d.	1.05 ± 0.06	14.4 ± 0.2	n.d.	n.d
K_2O	n.d.	n.d.	–	n.d.	n.d.
CaO	0.12 ± 0.05	22.7 ± 0.2	–	53.0 ± 0.6	46.4 ± 0.5
TiO_2	n.d.	0.10 ± 0.1	0.70 ± 0.03	–	–
V_2O_3	n.d.	n.d.	0.67 ± 0.02	–	–
Cr_2O_3	0.03 ± 0.06	0.75 ± 0.06	50.8 ± 0.5	0.05 ± 0.09	n.d.
MnO	0.35 ± 0.04	0.15 ± 0.04	0.35 ± 0.02	n.d.	n.d.
FeO	31.9 ± 0.4	6.09 ± 0.16	27.0 ± 0.4	0.9 ± 0.1	1.19 ± 0.03
CoO	n.d.	n.d.	n.d.	–	–
NiO	n.d.	n.d.	n.d.	n.d.	n.d.
ZnO	–	–	0.25 ± 0.10	–	–
Cl	–	–	–	4.7 ± 0.2	n.d.
F	–	–	–	0.9 ± 0.2	n.d.
H_2O[a]				*0.14*	
Total	100.0	100.3	99.1	101.4	99.9
–O=F				0.38	
–O=Cl				1.06	
New Total				100.0	

[a]H_2O (OH) value is based on stoichiometry.

n signifies the number of points analyzed. n.d. denotes that the elements were analyzed, but not detected. – denotes that the element was not analyzed. The total cation count and charge balancing suggests no Fe^{3+} in the chromite.

Chlorapatite is common in brachinites (e.g., Nehru et al. 1992), and is present in NWA 4872 (Table 2), with 4.7 ± 0.2 wt% Cl and 0.9 ± 0.2 wt% F, with inferred total H_2O (OH) based on stoichiometry of approximately 0.1 wt%. A small amount of merrillite (Table 2) and Fe-phosphate (Table 3) is present around some of the chlorapatite. The Fe-phosphate gave low totals probably due to the presence of OH, H_2O, and/or excess O in its structure. As with many fine grain materials, porosity and poor surface quality can also result in low totals; however, the consistent values obtained from multiple points suggest that this is not an issue here. EMP analyses of the marcasite have low totals, suggesting the presence of excess oxygen (Table 3), which is consistent with it representing a terrestrial weathering product and forming in association with oxidation products. The oxygen is probably included in small amounts of surrounding Fe-oxide (-hydroxide) that overlapped under the electron beam. Analysis of the Fe-oxides also had low totals (Table 3), probably due to mixing of phases and the presence of goethite and silicates in these mixtures. Quantitative analysis of goethite was not possible because it was only present in mixtures with other weathering products and areas where the beam would overlap adjacent phases. The identification of goethite was only possible with Raman analysis.

Trace Element Analysis

Abundances of the REE were determined for pyroxene, olivine, and chlorapatite using LA-ICP-MS (Fig. 6; Table 4). The low concentrations of the REE in olivine required the use of a large beam diameter (80 μm) and only a partial pattern was obtained. The small size of the chlorapatite grains did not allow for a large beam size (25 μm), which also resulted in a partial REE pattern, due to the small amount of total analyte measured. Single grain REE abundances (this study) have been plotted with bulk-rock CI chondrite normalized REE abundances (Day et al. 2012a) in Fig. 6. Pyroxenes have HREE>LREE, as also appears to be the case for olivine. A similar trend is also apparent in the bulk rock. The olivine has subchondritic absolute abundances of the REE and has similar concentrations to that of the whole rock, suggesting that the bulk-rock pattern is dominated by the large amount of olivine present. Chlorapatite has the highest REE concentrations measured in the sample and appears to only weakly influence the bulk-rock pattern, suggesting that it is a minor phase in the bulk rock as a whole. The bulk-rock REE pattern for NWA 4872 has a lower absolute REE content than any other measured brachinite consistent with limited interstitial REE-rich phosphate phases and the dominant control of olivine.

Table 3. Representative compositions for weathering products in NWA 4872.

wt%	Marcasite[a]	Hematite[b]	Magnetite[b]	Fe-Phosphate (n = 4)	
Si	*0.08*	4.48	0.2	1.0 ± 0.2	SiO_2
P	–	–	–	28.7 ± 0.7	P_2O_5
Na	–	–	–	n.d.	Na_2O
Mg	*0.06*	0.19	n.d.	1.6 ± 0.3	MgO
K	–	–	–	0.05 ± 0.03	K_2O
Ca	–	–	–	0.3 ± 0.1	CaO
V	*0.02*	n.d.	n.d.	–	V_2O_3
Mn	*n.d.*	n.d.	n.d.	0.44 ± 0.05	MnO
Fe	*48.3*		30.0	50.3 ± 0.9	FeO
		88.2	66.4	–	Fe_2O_3
Co	*0.05*	n.d.	0.16	–	CoO
Ni	*0.32*	0.56	0.23	n.d.	NiO
Cl	*n.d.*	–	–	0.03 ± 0.02	Cl
S	*45.6*	–	–	–	
Total	*94.4*	93.4	97.0	82.4	

n signifies the number of points analyzed for the Fe-phosphate. Italicized values are elemental percent, while all others are oxide percent. The values for FeO and Fe_2O_3 in magnetite were arrived at by forcing the total cation count in the formula to equal 3.

[a]Microprobe and Raman data suggest that marcasite is the dominant phase. However, other sulfide phases may be present in the analyzed region. The representative analysis here is an example with relatively high totals. Many analyses had lower totals due to the presence of oxygen in the weathered grains.

[b]Most analyzed points were determined to be mixtures. The representative analyses here are taken from an area dominated by each Fe-oxide. Some silicate contamination is present and other weathering products may also be present.

All HSE abundances in the Cr-spinel grains were below the limits of detection (typically <1 ppm). Absolute abundances of the HSE in sulfide and alteration phases were difficult to quantitatively determine by LA-ICP-MS due to the variable degrees of alteration, which prevents accurate normalization of the LA-ICP-MS to EMP data. Laser spots were placed in areas dominated by a single phase (e.g., Fig. 5), Fe-sulfide or Fe-oxide, but ultimately measured a mixture of the targeted phase and associated weathering products. Thus, the propagated uncertainties in absolute abundance from uncertainties in major-element normalization (typically Fe) can exceed 50%. Nonetheless, the relative abundances can be confidently established (Fig. 7) and can be compared with fresh troilite analyzed in past work on brachinites (Day et al. 2012a).

DISCUSSION

Fluid–Rock Interaction in NWA 4872

The fluid–rock interactions experienced by NWA 4872 occurred in two stages. The first stage occurred on the parent body and the second occurred at low temperatures, probably on Earth. Shearer et al. (2011) report that the merrillite in GRA 06128/9 is magmatic in origin and that chlorapatite formed from interaction between merrillite and a Cl-rich melt residuum or lower temperature fluid on the parent body. A similar scenario could have existed for brachinites.

Calcite is found on the exterior of the 23.55 g piece of NWA 4872 and in large cracks around the exterior of ROMB-1, consistent with low-temperature alteration. However, ROMB-2 and the remainder of ROMB-1 show no further carbonate precipitation. This may suggest, as terrestrial fluids penetrated into the meteorite, that sulfide and chlorapatite were weathered producing sulfuric and hydrochloric acid. This chemical alteration can change the types of alteration and mineral precipitation occurring on the interior and is consistent with a lack of calcite in NWA 4872. A scenario of terrestrial weathering is more likely than extraterrestrial alteration, especially given that other brachinites contain unaltered troilite. The observed type of alteration is consistent with a desert environment in which low water–rock ratios and weathering, largely of sulfides, occur for short time periods.

The bulk density determined by CT is consistent with values found for other brachinites using the Archimedean "glass bead" method (3.1–3.9 g cm^{-3}, Macke et al. 2011). Brachinites measured by Macke et al. (2011) had porosities ranging from insignificant values, up to approximately 15% (Eagles Nest). Small fractures in ROMB-1 can be interpreted as porous "pathways" for water and weathering, but were too small to be observed in 3-D with micro-CT and many of the cracks are probably filled in with weathering product.

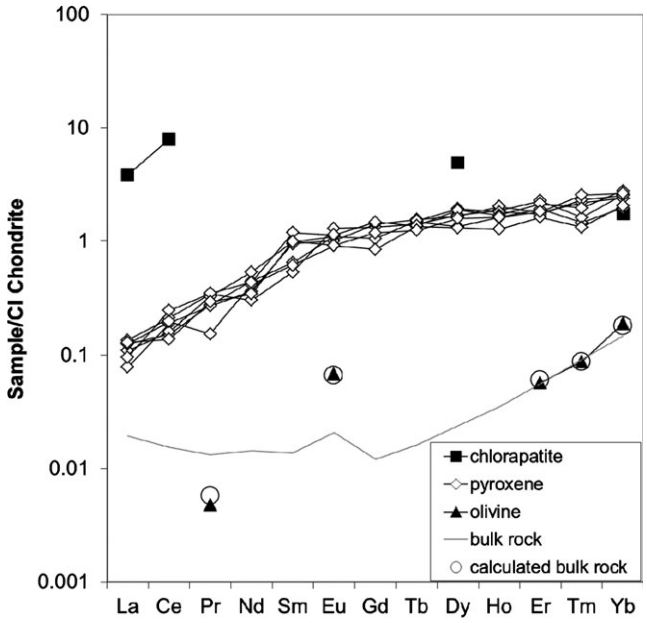

Fig. 6. Rare earth element abundances of phases in NWA 4872. The bulk-rock pattern from Day et al. (2012a) is shown in gray. CI chondrite normalization values taken from McDonough and Sun (1995).

The Formation of Marcasite and Major-Element Mobilization During Weathering

The production of FeS_2 from troilite requires sulfuric acid (Jerz and Rimstidt 2003; King and McSween 2005), which would have been produced during the interaction of water with sulfide grains in NWA 4872. The conversion of initial troilite to marcasite and Fe-oxide (-hydroxide) is deduced from Raman maps (Fig. 5). Troilite weathering resulted in the mobilization of S in the grains. Remnants of the troilite grains now consist of S-rich regions—marcasite (minor pyrrhotite/pyrite) and S-poor regions—hematite, magnetite, and goethite. An important consideration when analyzing mixtures with Raman spectroscopy is that some minerals are more Raman active than others. To positively identify marcasite as the main phase, it was necessary to also have EMP data.

The mobility of S and the formation of marcasite are not unique to NWA 4872. Weathered ordinary chondrites also contain marcasite (Al-Kathiri et al. 2005) and sulfur mobilization from troilite has been observed in ordinary chondrites exposed to hot desert weathering (Lee and Bland 2004). Martian meteorites also contain marcasite. Pyrite with lamellae of marcasite was reported in the nakhlite Lafayette (Boctor et al. 1976), the Sayh al Uhaymir 094 shergottite includes pyrrhotite partially altered to marcasite and Fe-hydroxides (Gnos et al. 2002), and marcasite is the dominant sulfide in Chassigny (Floran et al. 1978; Rochette et al. 2001). The marcasite in Lafayette has been considered as martian in origin (Boctor et al. 1976), but, in general, marcasite in meteorites is considered to be terrestrial alteration. Miller Range nakhlites have regions of alteration of pyrrhotite to Fe-oxide and S mobility (Day et al. 2006b; Hallis and Taylor 2011). This association is somewhat comparable to the weathering in NWA 4872. Day et al. (2006b) and Hallis and Taylor (2011), however, consider the alteration in MIL 03346 and relatives to be martian in origin.

Major-element mobilization in NWA 4872 also resulted in the formation of Fe-phosphate from initial chlorapatite. This phase appears to be similar to that found in the brachinite Eagles Nest. Swindle et al. (1998) proposed that the mineral is ludlamite ($[Fe,Mg,Mn]_3[PO_4]_2 \cdot 4H_2O$), from chemical comparisons. However, the Raman spectrum of the Fe-phosphate in

Table 4. Trace element abundances for silicates and chlorapatite in NWA 4872.

ppm	Olivine (n = 1)	Pyroxene (n = 7)	Chlorapatite (n = 1)	Bulk rock[a]
Sc	6.3	105 ± 4	<10.24	4.68
Ti	18.1	598 ± 19	–	54.2
V	19.9	424 ± 7	–	55.2
Cr	292	5049 ± 164	–	3293
Ga	<0.63	5.5 ± 0.3	–	1.8
Ge	<4.22	12 ± 5	–	6.90
Rb	<0.64	<0.43	–	0.049
Sr	<10.26	<35.74	410.0	0.74
Y	0.018	2.3 ± 0.2	3.7	0.052
Zr	0.011	0.76 ± 0.05	<1.08	0.132
Nb	n.d.	<0.03	0.1	0.0116
Ba	<0.91	<0.99	–	0.68
La	n.d.	0.027 ± 0.005	0.9	0.0046
Ce	n.d.	0.11 ± 0.02	4.9	0.0094
Pr	0.00044	0.027 ± 0.006	<0.75	0.0012
Nd	n.d.	0.19 ± 0.04	<3.69	0.0065
Sm	n.d.	0.13 ± 0.04	<2.19	0.0020
Eu	0.0038	0.06 ± 0.01	<10.64	0.0012
Gd	n.d.	<0.30	<6.72	0.0084
Tb	n.d.	0.051 ± 0.004	<1.18	0.0006
Dy	n.d.	0.40 ± 0.06	1.2	0.0059
Ho	<0.08	0.09 ± 0.01	<0.91	0.0019
Er	0.0091	0.30 ± 0.04	<8.07	0.0090
Tm	0.0022	0.04 ± 0.01	<2.77	0.0023
Yb	0.030	0.39 ± 0.05	0.3	0.0238
Lu	0.0052	<0.10	<0.35	0.0057
Hf	n.d.	0.04 ± 0.02	n.d.	0.0031
Ta	n.d.	0.0011 ± 0.0004	n.d.	0.0031
Pb	0.080	<0.42	<0.33	0.085
Th	n.d.	<0.003	0.2	0.001
U	n.d.	0.0005 ± 0.0004	0.1	0.0005

[a]Bulk-rock analyses from Day et al. (2012a).
n signifies the number of points analyzed.

this study (see supporting information) does not match that of ludlamite. Instead, it suggests a nearly or completely amorphous phase. Here, the phase's association with weathering pathways, sulfate formation, and its low EMP totals suggest a weathering paragenesis. However, a more complex history of shock melting followed by weathering of the surrounding material cannot be excluded.

In general silicate alteration appears to be minimal in NWA 4872. Raman analysis did confirm the formation of magnesium sulfate in a few locations. The magnesium in this phase could be the result of minor silicate breakdown. Fine-grained Fe-oxide and olivine were also present, perhaps suggesting the start of olivine alteration as seen in terrestrial olivine by Kuebler et al. (2003, 2004) and in nakhlites (e.g., Bridges and Grady 2000; Day et al. 2006b; Hallis and Taylor 2011; Kuebler et al. 2004). However, clay formation could not be confirmed, suggesting that the magnesium content more likely originated from the terrestrial environment.

Weathering Effects on the REE, HSE, and Re/Os Ratio in Brachinites

Bulk analysis of Eagles Nest determined that it has a high LREE-enrichment and negative Ce-anomaly (Swindle et al. 1998), consistent with terrestrial weathering. Single grains of apatite and olivine in Eagles Nest have the same trend (Crozaz et al. 2003). High levels of Ba, Sr, and/or Pb are present in bulk analyses of Elephant Morraine 99402, Brachina, and NWA 4882. In contrast, NWA 4872 has relatively low abundances of these elements (Day et al. 2012a). LA-ICP-MS analyses of olivine, pyroxene, and minor chlorapatite grains allow comparison of modally recombined REE abundances with the measured bulk rock and are similar (Fig. 6), indicating that the REE in NWA 4872 have not been disturbed by weathering, and that NWA 4872 has been negligibly modified compared with some brachinites. The bulk-rock LREE contents of NWA 4872 also suggest limited modification by terrestrial weathering (Table 4; Fig. 6) (Day et al. 2012a), consistent with the primary weathering of NWA 4872 being sulfide and metal breakdown.

The HSE abundances measured for sulfide and sulfide by-product mineral grains in NWA 4872 vary significantly. However, the positive Ru "anomaly" (depleted Ir, Pt, and Pd relative to Ru) reported in Day et al. (2012a) is a common feature between mineral grains semiquantitatively analyzed in this study (Fig. 7). Thus, despite relatively extensive sulfide weathering, the relative abundances of the HSE, and interelement fractionations of these elements, remain a faithful representation of processes acting on NWA 4872's parent body. However, grain-to-grain variations in Re and Os concentrations from weathering account for differences in Re/Os ratios observed in separate splits of NWA 4872 (Day et al. 2012a).

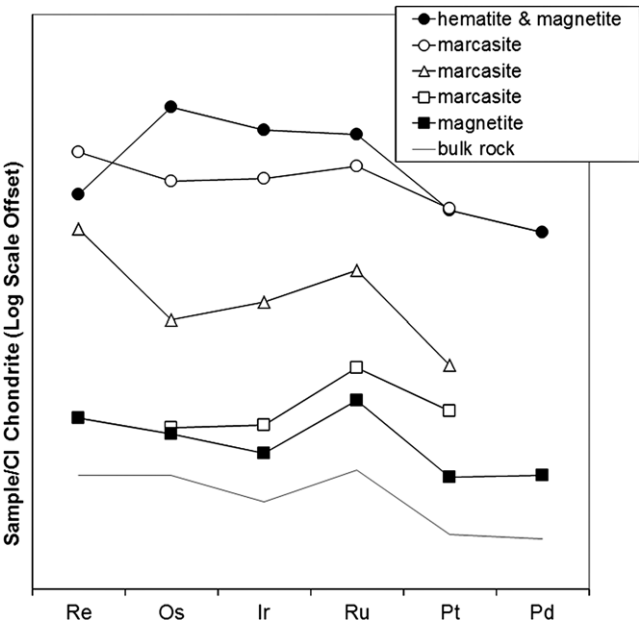

Fig. 7. Representative HSE abundances from weathered grains compared with the bulk-rock pattern for NWA 4872 (from Day et al. 2012a). Patterns marked with the same geometric shape represent two areas of the same grain. CI chondrite normalization values taken from McDonough and Sun (1995).

A region containing marcasite, hematite, and magnetite (Fig. 7) shows a marked decrease in Re relative to Os in the oxides relative to the marcasite. In some cases (e.g., Fig. 7, triangles), grains containing dominantly marcasite have a relatively elevated Re/Os ratio compared with the bulk-rock Re/Os. Oxidative removal of Re and the formation of sulfides with high Re in NWA 4872 appear to be the cause of these variations and similar trace element mobility has been seen in terrestrial rocks (e.g., Reisberg et al. 2008). A single analysis of a region dominated by magnetite (Fig. 7) has relative abundances of the HSE similar to that of bulk brachinite analyses.

According to the Raman maps in this study, up to 9% of NWA 4872 is currently some form of weathering product. About 7% of the section is Fe-oxide (-hydroxide) and 2.3% is altered sulfide, such as marcasite. These values suggest that oxidation is the dominant weathering effect and so the bulk HSE abundances would be expected to be disturbed mostly by Re loss and, potentially, Os uptake. This appears to be the case for many brachinites (Day et al. 2012a). Sulfide weathering is a likely source of Re-Os isotope disturbance in olivine-dominated achondrites, such as NWA 4872,

brachinites, and brachinite-like achondrites (Day et al. 2012a), ureilites (Rankenburg et al. 2007, 2008) and diogenites (Day et al. 2012b), where disturbance of the Re-Os isotope system has been observed previously. Sulfide weathering may also be important in other achondrites and chondrites which are not olivine-dominated, but, nonetheless, have Re and Os that are primarily hosted in sulfide or metal phases (e.g., Walker et al. 2002; Day et al. 2007; Brandon et al. 2012; Riches et al. 2012; Van Acken et al. 2012).

Effects of Heterogeneous Mineral Distribution on Interpretation of Bulk Trace Element Composition

In polished-section ROMB-2, the heterogeneous distribution of high-density phases is visible (Fig. 1). However, CT analysis of a larger mass in 3-D gives a better understanding of the heterogeneity in the sample, accentuating the uneven distribution of high-density phases (Fig. 1). It should be noted that the micro-CT analyses in this study only image large grains (>~150 μm) and that the contrast in density for the technique we applied needs to be significant. For example, Fe-sulfide and Fe-oxide (-hydroxide) phases are often not imaged and pyroxene and olivine are indistinguishable from one another. The heterogeneous distribution of high-density phases in NWA 4872 re-emphasizes the mode effect on precious, low-availability sample mass rocks. This effect describes where nonrepresentative volumes of rock are chosen for analysis, resulting in greater variability in chemical measurements (e.g., Rankenburg et al. 2007, 2008; Spicuzza et al. 2007). The mode effect is particularly problematic for coarse-grained rocks. As sectioning is typically done in an arbitrary manner, for most meteorites, there is a danger that either an unrepresentative sample may be produced or, conversely, interesting components may be missed. This in turn can lead to errors in calculated whole-rock trace element abundances gained from micro-analytical techniques (i.e., LA-ICP-MS, SIMS) derived from modal recombination. In the ROMB-2 section, a large Cr-spinel grain suggests that the uncertainty in Cr-spinel modal abundance is of the order of ±0.8% for samples of this size.

Unlike the difficulties in quantifying the total HSE budget of NWA 4872 from weathered sulfide, we were able to perform whole-rock REE pattern modal recombination (Fig. 6). Modal percentages gained from Raman mapping were used and the overall pattern is largely influenced by olivine, which dominates the sample (89%). The olivine data collected here are limited due to the low REE abundances and minor phases (e.g., phosphates) are not accounted for due to their low modal values, which could not be accurately measured by Raman mapping. However, the calculated values, along with the measured bulk-rock REE values clearly show the dominant influence of olivine. Our new results therefore add observational support to the idea that complications can result from heterogeneous phase distribution, but this mode effect has not had an effect on bulk REE data collected on NWA 4872 thus far.

Determining Primary Parent-Body Processes from the Weathered NWA 4872

NWA 4872 contains no observable plagioclase and exhibits the lowest bulk concentrations of the REE of any brachinite (Day et al. 2012a). These properties suggest that it is the best current representation of a residuum from the melt processes that are thought to have occurred on the brachinite parent body. The REE pattern for pyroxene in this study is similar to that of EET 99402 and GRA 06128 (Day et al. 2012a). High-Ca pyroxenes from all three have a convex pattern from La to Lu (light to heavy REE). The high-Ca pyroxenes in this study do not exhibit the negative Eu-anomalies observed in GRA 06129 and the brachinite-like achondrite NWA 5400 (Day et al. 2012a). The absence of a negative Eu-anomaly suggests that the pyroxene grains in NWA 4872 are residual and did not form during or following the partial melting event that extracted felsic and Fe, Ni, and S-rich melts. The minor positive Eu-anomaly in the bulk-rock analysis (Day et al. 2012a; $Eu/Sm_n = 3.5$, where n = CI-chondrite normalized) is likely the result of minor and unobserved plagioclase or plagioclase-composition glass in melt inclusions, as observed in Brachina (Nehru et al. 1983).

Recommendations for Analysis of Weathering Products and Heterogeneous Meteorites

Analysis of the weathering products in NWA 4872 made use of a number of techniques recommended for use with hydrous iron sulfates (Hyde et al. 2011). The methods suggested for these sulfate minerals apply to a number of weathering products that are beam- and/or vacuum-sensitive. Micro-Raman spectroscopy with low laser power, and similar techniques, allows successful elucidation of weathering products, including hydrous phases (e.g., Hallis and Taylor [2011] and this study). Raman mapping also allowed for determination of modal abundances of weathering product. This is an important measurement that is often neglected in meteoritics. The low vacuum SEM mapping provided a view of the distribution of major and minor elements. This technique can be considered nondestructive for most phases present in achondritic meteorites. However, phases such as hydrated weathering products could be vacuum- and/or beam-sensitive. If highly hydrated minerals are expected,

this should be used following initial surveys using other techniques such as micro-Raman. In this study, Raman analyses were performed before and after SEM and LA-ICP-MS work. The sulfide and Fe-oxide (-hydroxide) weathering assemblages were not affected by these analyses (except for perhaps in the LA-ICP-MS analysis pit). It should be noted that the small amounts of Fe-phosphate, anhydrite, and Mg-sulfate were not found with Raman prior to SEM work and elemental mapping. There is, therefore, uncertainty in the initial hydration state of these minerals. Milling of samples using a FIB can be monitored in real time and in this study showed no textural changes to volatile-rich phases. This type of sample preparation could be advantageous for future studies of weathering products in meteorites using EBSD. The micro-CT techniques used here could be applied to the study of weathering products in meteorites; however, the small size of most weathering features and the large size of many meteorites are limiting factors. Micro-CT is uniquely suitable for observing phase distribution in meteorite interiors (e.g., McCoy et al. 2006). Targeted cutting, using micro-CT volumes for direction, can expose previously unseen features and can help constrain uncertainty in modal abundance values. For rare and valuable samples, targeted cutting provides the maximum amount of information from a sample with the fewest number of cuts. The work done here used end-cut material, which is typical for sectioning and bulk analysis, making it relevant to the effects of weathering and phase distribution on typical study material. Future work using these techniques would benefit from comparing multiple meteorites and/or interior cuts versus exterior cuts from single meteorites.

CONCLUSIONS

Weathering of achondrite meteorite finds involves complex physical and chemical modifications that can hamper investigations of extraterrestrial characteristics. Phase distribution in some coarsely grained meteorites, for which limited material may be available, can lead to uncertainties relating to compositional representativeness. Investigation of brachinite NWA 4872 confirms that weathering has redistributed sulfur from primary troilite, resulting in the formation of Fe-oxide (-hydroxide) and marcasite. Measurement of altered sulfide and Fe-oxide, reveal grain-to-grain variations of Re and Os, but the relative abundances of the other HSE in these grains are broadly parallel to the bulk-rock composition. These new results support evidence from a range of chondrite and achondrite meteorite studies that Re and Os mobilize during terrestrial weathering of sulfides. Single grain REE patterns indicate a heritage as a residuum after partial melting on the brachinite parent body(ies). Microcomputed tomography shows that high-density regions and heterogeneities in mineral distribution occur. Nonetheless, we find that the bulk-rock compositions measured for NWA 4872 on fragments (Day et al. 2012a) appear to be reasonable representations of composition, but that smaller sample sizes may bias composition due to heterogeneous phase distribution.

Acknowledgments—We are grateful to David Gregory, Joseph Umoh, David Edey, Ivan Barker, Ian Nicklin, Phil McCausland, and James Brenan for their assistance with this work and Marc Fries, Cyrena Goodrich, Lydia Hallis, Jason Herrin, and Klaus Keil for constructive review comments. For analytical assistance, we thank the Great Lakes Institute for Environmental Research at University of Windsor, the Western University Nanofabrication Facility, and the microprobe facilities at the University of Toronto and Queen's University. We also thank ROM donors for their financial contributions to the new laboratory at the Royal Ontario Museum. This research was partially supported by funding from the NASA Cosmochemistry program to JMDD (NNX12AH75G) and a NSERC Discovery grant (KTT).

Editorial Handling—Dr. Cyrena Goodrich

REFERENCES

Achterberg E. V., Ryan C. G., Jackson S. E., and Griffin W. L. 2001. Appendix 3: Data reduction software for LA-ICP-MS. In *Laser ablation-ICP-MS in the earth sciences*, edited by Sylvester P. *Short Course Series* 29:239–243.

Al-Kathiri A., Hofmann B. A., Jull A. J. T., and Gnos E. 2005. Weathering of meteorites from Oman: Correlation of chemical and mineralogical weathering proxies with ^{14}C terrestrial ages and the influence of soil chemistry. *Meteoritics & Planetary Science* 40:1215–1239.

Ash R. D. and Pillinger C. T. 1995. Carbon, nitrogen and hydrogen in Saharan chondrites: The importance of weathering. *Meteoritics* 30:85–92.

Boctor N. Z., Meyer H. O. A., and Kullerud G. 1976. Lafayette meteorite: Petrology and opaque mineralogy. *Earth and Planetary Science Letters* 32:69–76.

Brandon A. D., Puchtel I. S., Walker R. J., Day J. M. D., Irving A. J., and Taylor L. A. 2012. Evolution of the Martian mantle inferred from the ^{187}Re-^{187}Os isotope and highly siderophile element abundance systematics of shergottite meteorites. *Geochimica et Cosmochimica Acta* 76:206–235.

Bridges J. C. and Grady M. M. 2000. Evaporite mineral assemblages in the nakhlites (Martian) meteorites. *Earth and Planetary Science Letters* 176:267–279.

Chou I.-M. and Seal R. R. II. 2003. Determination of epsomite-hexahydrite equilibria by the humidity-buffer technique at 0.1 MPa with implications for phase equilibria in the system $MgSO_4 \cdot H_2O$. *Astrobiology* 3:619–630.

Connolly H. C. Jr., Smith C., Benedix G., Folco L., Righter K., Zipfel J., Yamaguchi A., and Chennaoui Aoudjehane

H. 2007. The Meteoritical Bulletin, No. 93. *Meteoritics & Planetary Science* 43:571–632.

Cooney T. F., Scott E. R. D., Krot A. N., Sharma S. K., and Yamaguchi A. 1999. Vibrational spectroscopic study of minerals in the Martian meteorite ALH 84001. *American Mineralogist* 84:1569–1576.

Crozaz G., Floss C., and Wadhwa M. 2003. Chemical alteration and REE mobilization in meteorites from hot and cold deserts. *Geochimica et Cosmochimica Acta* 67:4727–4741.

Day J. M. D., Floss C., Taylor L. A., Anand M., and Patchen A. D. 2006a. Evolved mare basalt magmatism, high Mg/Fe feldspathic crust, chondritic impactors and the petrogenesis of Antarctic lunar meteorites Meteorite Hills 01210 and Pecora Escarpment 02007. *Geochimica et Cosmochimica Acta* 70:5957–5989.

Day J. M. D., Taylor L. A., Floss C., and McSween Y. 2006b. Petrology and chemistry of MIL 03346 and its significance in understanding the petrogenesis of nakhlites on Mars. *Meteoritics & Planetary Science* 41:581–606.

Day J. M. D., Pearson D. G., and Taylor L. A. 2007. Highly siderophile element constraints on accretion and differentiation of the Earth-Moon system. *Science* 315:217–219.

Day J. M. D., Ash R. D., Liu Y., Bellucci J. J., Rumble D. III, McDonough W. F., Walker R. J., and Taylor L. A. 2009. Early formation of evolved asteroidal crust. *Nature* 457:179–182.

Day J. M. D., Walker R. J., Ash R. D., Liu Y., Rumble D., III, Irving A. J., Goodrich C. A., Tait K. T., McDonough W. F., and Taylor L. A. 2012a. Origin of Graves Nunataks 06128 and 06129, brachinites, and brachinite-like achondrites by partial melting of volatile-rich primitive parent bodies. *Geochimica et Cosmochimica Acta* 81:94–128.

Day J. M. D., Walker R. J., Qin L., and Rumble D. 2012b. Late accretion as a natural consequence of planetary growth. *Nature Geoscience* 5:614–617.

de Faria D. L. A. and Lopes F. N. 2007. Heated goethite and natural hematite: Can Raman spectroscopy be used to differentiate them? *Vibrational Spectroscopy* 45:117–121.

de Faria D. L. A., Silva S. V., and de Oliveira M. T. 1997. Raman microspectroscopy of some iron oxides and oxyhydroxides. *Journal of Raman Spectroscopy* 28:873–878.

Floran R. J., Prinz M., Hlava P. F., Keil K., Nehru C. E., and Hinthorne J. R. 1978. The Chassigny meteorite: A cumulate dunite with hydrous amphibole-bearing melt inclusions. *Geochimica et Cosmochimica Acta* 42:1213–1229.

Gnos E., Hofmann B., Franchi I. A., Al-Kathiri A., Huser M., and Moser L. 2002. Sayh al Uhaymir 094: A new Martian meteorite from the Oman Desert. *Meteoritics & Planetary Science* 37:835–854.

Goodrich C. A. 1998. Brachinites: Residues from low degrees of melting of a heterogeneous parent body (abstract). *Meteoritics & Planetary Science* 33:A60.

Goodrich C. A. and Lugmair G. W. 1995. Stalking the LREE-enriched component in ureilites. *Geochimica et Cosmochimica Acta* 59:2609–2620.

Guan Y. and Crozaz G. 2000. LREE-enrichments in ureilites: A detailed ion microprobe study. *Meteoritics & Planetary Science* 35:131–144.

Hallis L. J. and Taylor G. J. 2011. Comparisons of the four Miller Range nakhlites, MIL 03346, 090030, 090032 and 090136: Textural and compositional observations of primary and secondary mineral assemblages. *Meteoritics & Planetary Science* 46:1787–1803.

Herman G. T. 1979. Correction for beam hardening in computed tomography. *Physics in Medicine and Biology* 24:81–106.

Hyde B. C., King P. L., Dyar M. D., Spilde M. N., and Ali A.-M. S. 2011. Methods to analyze metastable and microparticulate hydrated and hydrous iron sulfate minerals. *American Mineralogist* 96:1856–1869.

Izawa M. R. M., Flemming R. L., Banerjee N. R., and Matveev S. 2011. QUE 94204: A primitive enstatite achondrite produced by the partial melting of an E chondrite-like protolith. *Meteoritics & Planetary Science* 46:1742–1753.

Jerz J. K. and Rimstidt J. D. 2003. Efflorescent iron sulfate minerals: Paragenesis, relative stability, and environmental impact. *American Mineralogist* 88:1919–1932.

Jolliff B. L., Hughes J. M., Freeman J. J., and Zeigler R. A. 2006. Crystal chemistry of lunar merrillite and comparison to other meteoritic and planetary suites of whitlockite and merrillite. *American Mineralogist* 91:1583–1595.

King P. L. and McSween H.Y., Jr. 2005. Effects of H_2O, pH, and oxidation state on the stability of Fe minerals on Mars. *Journal of Geological Research* 110:E12S10, doi:10.1029/2005JE002482.

Kuebler K. E., Wang A., Haskin L. A., and Jolliff B. L. 2003. A study of olivine alteration to iddingsite using Raman spectroscopy (abstract #1953). 34th Lunar and Planetary Science Conference. CD-ROM.

Kuebler K. E., Jolliff B. L., Wang A., and Haskin L. A. 2004. A survey of olivine alteration products using Raman spectroscopy (abstract #1704). 35th Lunar and Planetary Science Conference. CD-ROM.

Laetsch T. and Downs R. 2006. Software for identification and refinement of cell parameters from powder diffraction data of minerals: Using the RRUFF project and American Mineralogist Crystal Structure Databases. 19th General Meeting of the International Mineralogical Association.

Lee M. R. and Bland P. A. 2004. Mechanisms of weathering of meteorites recovered from hot and cold deserts and the formation of phylosilicates. *Geochimica et Cosmochimica Acta* 68:893–916.

Macke R. J., Britt D. T., and Consolmagno G. J. 2011. Density, porosity, and magnetic susceptibility of achondritic meteorites. *Meteoritics & Planetary Science* 46:311–326.

McCausland P. J. A., Brown P. G., and Holdsworth D. W. 2010. Rapid reliable acquisition of meteorite volumes and internal features by laboratory X-ray micro-CT scanning (abstract #2584). 41st Lunar and Planetary Science Conference. CD-ROM.

McCoy T. J., Keil K., Muenow D. W., and Wilson L. 1997. Partial melting and melt migration in the acapulcoite-lodranite parent body. *Geochimica et Cosmochimica Acta* 61:639–650.

McCoy T. J., Carlson W. D., Nittler L. R., Stroud R. M., Bogard D. D., and Garrison D. H. 2006. Gaves Nunataks 95209: A snapshot of metal segregation and core formation. *Geochimica et Cosmochimica Acta* 70:516–531.

McDonough W. F. and Sun S.-S. 1995. The composition of the Earth. *Chemical Geology* 120:223–253.

Mernagh T. P. and Trudu A. G. 1993. A laser Raman microprobe study of some geologically important sulphide minerals. *Chemical Geology* 103:113–127.

Nehru C. E., Prinz M., Delaney J. S., Dreibus G., Palme H., Spettel B., and Wänke H. 1983. Brachina: A new type of meteorite, not a Chassignite. 14th Lunar and Planetary Science Conference. *Journal of Geophysical Research* 88: B237–B244.

Nehru C. E., Prinz M., Weisberg M. K., Ebihara M. E., Clayton R. N., and Mayeda T. K. 1992. Brachinites: A new primitive achondrite group (abstract). *Meteoritics* 27:267.

Otsu N. 1979. A threshold selection method from gray-level histograms. *Transactions IEEE on Man Systems, and Cybernetics SMC-9* 1:62–66.

Rankenburg K., Brandon A. D., and Humayun M. 2007. Osmium isotope systematics of ureilites. *Geochimica et Cosmochimica Acta* 71:2402–2413.

Rankenburg K., Humayun M., Brandon A. D., and Herrin J. S. 2008. Highly siderophile elements in ureilites. *Geochimica et Cosmochimica Acta* 72:4642–4659.

Rasband W. S. *ImageJ*. Bethesda, Maryland: U.S. National Institutes of Health. http://imagej.nih.gov/ij/, 1997–2012.

Reisberg L., Rouxel O., Ludden J., Staudigel H., and Zimmermann C. 2008. Re–Os results from ODP site 801: Evidence for extensive Re uptake during alteration of oceanic crust. *Chemical Geology* 248:256–271.

Riches A. J. V., Day J. M. D., Walker R. J., Simonetti A., Liu Y., Neal C. R., and Taylor L. A. 2012. Rhenium–osmium isotope and highly-siderophile-element abundance systematics of angrite meteorites. *Earth and Planetary Science Letters* 353–354:208–218.

Rochette P., Loran J.-P., Fillion G., and Sautter V. 2001. Pyrrhotite and the remanent magnetization of SNC meteorites: A changing perspective on Martian magnetism. *Earth and Planetary Science Letters* 190:1–12.

Rumble D., Irving A. J., Bunch T. E., Wittke J. H., and Kuehner S. M. 2008. Oxygen isotopic and petrological diversity among brachinites NWA 4872, NWA 4874, NWA 4882 and NWA 4969: How many ancient parent bodies? (abstract #1974). 39th Lunar and Planetary Science Conference. CD-ROM.

Sharma S. K., Misra A. K., Lucey P. G., and Lentz R. C. F. 2009. A combined remote Raman and LIBS instrument for characterizing minerals with 532 nm laser excitation. *Spectrochimica Acta Part A* 73:468–476.

Shearer C. K., Burger P. V., Neal C., Sharp Z., Spivak-Birndorf L., Borg L., Fernandes V., Papike J. J., Karner J., Wadhwa M., Gaffney A. M., Shafer J., Geissman J., Atudorei N.-V., Herd C., Weiss B. P., King P. L., Crowther S. A., and Gilmour J. D. 2010. Non-basaltic asteroidal magmatism during the earliest stages of solar system evolution. A view from Antarctic achondrites Graves Nunataks 06128 and 06129. *Geochimica et Cosmochimica Acta* 74:1172–1199.

Shearer C. K., Burger P. V., Papike J. J., Sharp Z. D., and McKeegan K. D. 2011. Fluids on differentiated asteroids: Evidence from phosphates in differentiated meteorites GRA 06128 and GRA 06129. *Meteoritics & Planetary Science* 46:1345–1362.

Spicuzza M. J., Day J. M. D., Taylor L. A., and Valley J. W. 2007. Oxygen isotope constraints on the origin and differentiation of the Moon. *Earth and Planetary Science Letters* 253:254–265.

Swindle T. D., Kring D. A., Burkland M. K., Hill D. H., and Boynton W. V. 1998. Noble gases, bulk chemistry, and petrography of olivine-rich achondrites Eagles Nest and Lewis Cliff 88763: Comparison to brachinites. *Meteoritics & Planetary Science* 33:31–48.

Tait K. T., Barkley M. C., Thompson R. M., Origlieri M. J., Evans S. H., Prewitt C. T., and Yang H. 2011. Bobdownsite, a new mineral species from Big Fish River, Yukon, Canada, and its structural relationship with whitlockite-type compounds. *Canadian Mineralogist* 49:1065–1078.

Van Acken D., Brandon A. D., and Lapen T. J. 2012. Highly siderophile element and osmium isotope evidence for postcore formation magmatic and impact processes on the aubrite parent body. *Meteoritics & Planetary Science* 47:1606–1623.

Walker R. J., Horan M. F., Morgan J. W., Becker H., Grossman J. N., and Rubin A. E. 2002. Comparative ^{187}Re-^{187}Os systematics of chondrites: Implications regarding early solar system processes. *Geochimica et Cosmochimica Acta* 23:4187–4201.

Wang A., Jolliff B. L., and Haskin L. A. 1999. Raman spectroscopic characterization of a Martian SNC meteorite: Zagami. *Journal of Geophysical Research* 104:8509–8519.

Wang A., Kuebler K. E., Jolliff B. L., and Haskin L. A. 2004. Raman spectroscopy of Fe-Ti-Cr-oxides, case study: Martian meteorite EETA79001. *American Mineralogist* 89:665–680.

Wang A., Freeman J. J., Jolliff B. L., and Chou I.-M. 2006. Sulfates on Mars: A systematic Raman spectroscopic study of hydration states of magnesium sulfates. *Geochimica et Cosmochimica Acta* 70:6118–6135.

Wang K., Day J. M. D., Korotev R. L., Zeigler R. A., and Moynier F. 2014. Iron isotope fractionation during sulfide-rich felsic partial melting in early planetesimals. *Earth and Planetary Science Letters* 392:124–132.

Weisberg M. K., Smith C., Benedix G., Folco L., Righter K., Zipfel J., Yamaguchi A., and Chennaoui Aoudjehane H. 2008. The Meteoritical Bulletin, No. 94. *Meteoritics & Planetary Science* 43:1551–1588.

White S. N. 2008. Laser Raman spectroscopy as a technique for identification of seafloor hydrothermal and cold seep minerals. *Chemical Geology*, doi:10.1016/j.chemgeo.2008.11.008.

Zeigler R. A., Korotev R., and Jolliff B. 2006. Geochemical signature of terrestrial weathering in hot-desert lunar meteorites (abstract). *Meteoritics & Planetary Science* 41 (supplement):A215.

Zeigler R. A., Jolliff B., Korotev R., Rumble D., Carpenter P. K., and Wang A. 2008. Petrology, geochemistry and likely provenance of unique achondrite Graves Nunatak 06128 (abstract #2456). 39th Lunar and Planetary Science Conference. CD-ROM.

SUPPORTING INFORMATION

Additional supporting information may be found in the online version of this article:

Data S1: Combined Raman and EBSD characterization technique.